PCCP

PAPER

Characterization of thin films of the solid electrolyte $Li_xMg_{1−2x}Al_{2+x}O_4$ (x = 0, 0.05, 0.15, 0.25)†

Brecht Put,*[ab] Philippe M. Vereecken,[ac] Maarten J. Mees,[a] Fabio Rosciano,[ad] Iuliana P. Radu[a] and Andre Stesmans[b]

RF-sputtered thin films of spinel $Li_xMg_{1−2x}Al_{2+x}O_4$ were investigated for use as solid electrolyte. The usage of this material can enable the fabrication of a lattice matched battery stack, which is predicted to lead to superior battery performance. Spinel $Li_xMg_{1−2x}Al_{2+x}O_4$ thin films, with stoichiometry (x) ranging between 0 and 0.25, were formed after a crystallization anneal as shown by X-ray diffraction and transmission electron microscopy. The stoichiometry of the films was evaluated by elastic recoil detection and Rutherford backscattering and found to be slightly aluminum rich. The excellent electronic insulation properties were confirmed by both current–voltage measurements as well as by copper plating tests. The electrochemical stability window of the material was probed using cyclic voltammetry. Lithium plating and stripping was observed together with the formation of a Li–Pt alloy, indicating that Li-ions passed through the film. This observation contradicted with impedance measurements at open circuit potential, which showed no apparent Li-ion conductivity of the film. Impedance spectroscopy as a function of potential showed the occurrence of Li-ion intercalation into the $Li_xMg_{1−2x}Al_{2+x}O_4$ layers. When incorporating Li-ions in the material the ionic conductivity can be increased by 3 orders of magnitude. Therefore it is anticipated that the response of $Li_xMg_{1−2x}Al_{2+x}O_4$ is more adequate for a buffer layer than as the solid electrolyte.

Li-ion batteries currently dominate the battery market of consumer products, thanks to their higher energy and power density than other battery chemistries.[1,2] Yet, to enable large scale use in new market segments, further improvement is needed.[3,4] In domains where safety and miniaturization are of key importance, opportunities are present for implementation of solid state thin film batteries.[5] Typical examples of these areas are medical implants, on chip storage, the Internet of things, body area networks, *etc.* The use of solid state thin-film batteries generally leads to an increased safety of operation and offers a wider temperature window,[6,7] improvements originating directly from the replacement of the liquid electrolyte by a solid state one. This eliminates the risk of leaking and reduces the temperature dependence of the ionic conductivity. Currently, the lack of solid electrolytes with a sufficiently high ion conductivity and wide electrochemical window is one of the main obstacles for the implementation of these devices.[4,8,9]

Typically, a solid electrolyte provides electronic insulation between the two electrodes thereby preventing self-discharge. Moreover, it also facilitates efficient Li-ion transport between the electrodes. The solid electrolyte, however, does not contribute to the energy content of the battery, so downscaling the electrolyte will increase the system's energy density. Currently the liquid electrolyte and the separator make up 15% of the mass, and approximately 10% of the volume, of the battery stack,[10,11] with a typical separator thickness of about 20 μm.[11,12] By replacing this with a nanometer sized solid electrolyte, a significant increase in volumetric energy density can be obtained.[13] Furthermore, the use of a solid electrolyte puts less stringent requirements on the packaging, so further gains might be obtained here by reducing packaging mass and cost.

Reducing the electrolyte's thickness also allows the use of materials with lower ionic conductivity. Indeed, the shorter diffusion length of the Li-ion between the battery electrodes, results in lower ionic resistance. For example, an electrolyte of 100 nm with a conductivity of $10^{−9}$ S $cm^{−1}$ has the same ionic resistance as a 100 μm one with a conductivity of $10^{−6}$ S $cm^{−1}$. This reasoning however only holds if a good contact can be ensured between the solid electrolyte and the electrode. It has been reported that the interfacial regions between the electrodes and the electrolyte can be over 50 nm in size.[14] This undoubtedly

[a] Imec, Kapeldreef 75, 3001 Leuven, Belgium. E-mail: brecht.put@imec.be
[b] KU Leuven Department of Physics and Astronomy, Celestijnenlaan 200D, 3001 Leuven, Belgium
[c] KU Leuven Centre for surface Chemistry and Catalysis, Kasteelpark Arenberg 23, 3001 Leuven, Belgium
[d] Toyota Europe – Hoge Wei 33 – Technical Centre B – 1930 Zaventem, Belgium
† Electronic supplementary information (ESI) available. See DOI: 10.1039/c5cp03916a

This journal is © the Owner Societies 2015

Phys. Chem. Chem. Phys., 2015, **17**, 29045–29056 | 29045

introduces an extra resistance, thus lowering the battery power output.[15]

To prevent the formation of these interface regions, it has been suggested to lattice match the battery components.[16] This should result in lithium conduction highways, giving rise to a high power output and therefore superior battery performance.[8,17,18] The lattice matching can also lead to an increased stability upon cycling since it can provide anchoring points for the electrodes.

Electrode materials with the spinel crystal structure are among the most promising electrodes currently known for lithium ion batteries.[19,20] As cathodes, a wide variety of doped $LiMn_2O_4$ forms have been described.[21,22] As a typical example of an anode material, the spinel structured $Li_4Ti_5O_{12}$ is often studied.[23,24] Both of these materials have a small volume change ($<3\%$[25]) upon lithium intercalation and a good capacity.[20]

However, good electrolytes with the spinel crystal structure are still lacking, although different spinels have already been studied in the past.[26–28] These typically have a limited electrochemical window (*e.g.* $Li_2MgTi_3O_8$ and $LiCoTi_3O_8$) and low ionic conductivity values, the highest reported value being 10^{-8} S cm^{-1} for $Li_2NiGe_3O_8$.[26] Recently, a new spinel electrolyte, $Li_xMg_{1-2x}Al_{2+x}O_4$, has been suggested by Rosciano *et al.*[8] It has a wide electrochemical window (0–10 V *vs.* Li$^+$/Li)[8] and powder nuclear magnetic resonance (NMR) measurements predict good ionic conductivity values. However, phase separation of the lithium rich compound into lithium blocking $LiAl_5O_8$ layers might occur for materials with high lithium content. These findings are confirmed by modeling where an increase in formation enthalpy with increasing lithium content has been inferred.[25]

In the present work, we describe the results on physical, electrical, and electrochemical characterization of RF-sputtered thin films of the spinel $Li_xMg_{1-2x}Al_{2+x}O_4$. Different stoichiometries ($x = 0$, 0.05, 0.15, 0.25) have been investigated for potential use as solid electrolyte. Electrical and ionic conductivity was determined in an unambiguous way. Evaluation of ionic conductivity in thin films is more straightforward compared with powder samples, as thin films inherently ensure good electrical contact and do not require a critical sintering step. Our work further focuses on the electrochemical characterization of the material and the variation of the ionic conductivity upon altering the potential difference across the electrolyte.

Experimental

Depositions of spinel layers were performed on an 80 nm thick platinum current collector. This layer was deposited by DC sputtering on a 10 nm thick TiN adhesion layer fabricated by atomic layer deposition. Underneath the adhesion layer, 30 nm of thermally grown SiO_2 was present as a barrier to prevent silicidation. Prior to the platinum deposition, the stack was subjected to a preannealing process at 800 °C in an atmosphere of 21% O_2 and 79% N_2, to prevent outgassing and recrystallization of the TiN layer in later stages of the experiment.

The $Li_xMg_{1-2x}Al_{2+x}O_4$ layers were deposited by RF sputtering (power 90 W, Ar flow 25 sccm, and pressure of 2.2×10^{-3} mBar) from a stoichiometric target. Four different stoichiometries have been investigated, namely $MgAl_2O_4$ ($x = 0$), $Li_{0.05}Mg_{0.9}Al_{2.05}O_4$ ($x = 0.05$), $Li_{0.15}Mg_{0.7}Al_{2.15}O_4$ ($x = 0.15$) and $Li_{0.25}Mg_{0.5}Al_{2.25}O_4$ ($x = 0.25$). Different film thicknesses were fabricated ranging from 20 nm to 600 nm. The layers were subjected to a crystallization anneal in an rapid thermal annealing oven (Annealsys) at 800 °C in an oxygen atmosphere. The morphology of the layers before and after annealing was checked by scanning electron microscopy (SEM, Nova). Transmission electron microscopy (TEM) was done using a Titan(FEI) operating at 120 kV.

Crystallinity was determined by X-ray diffraction (XRD) in the grazing incidence configuration (X'pert pro, Panalytical) using Cu Kα radiation. Compositional analysis of the layers was done using elastic recoil detection (ERD) and Rutherford backscattering (RBS). In ERD experiments, a primary ion beam of Cl^{4+} is accelerated to 6 MeV by a 2 MV tandem accelerator. The forward, recoiled and scattered ions are detected using a Time-of-flight-Energy (ToFE) telescope.[29] For these experiments, the $Li_xMg_{1-2x}Al_{2+x}O_4$ layers were deposited on a Si_3N_4 substrate to prevent interference from the underlying Pt layer.

All electrochemical testing involving lithium was done in an Ar glove box (O_2, H_2O < 1 ppm). The testing was carried out in a three electrode cell using Li foil as counter and reference electrodes. A solution of 1 M of $LiClO_4$ (battery grade, Sigma Aldrich) in propylene carbonate was used as the electrolyte. Electrochemical impedance spectroscopy (EIS) was performed at open circuit voltage (OCV) between 0.1 Hz and 1 MHz with an RMS amplitude of 10 mV using an autolab (Metrohm) potentiostat with a frequency response analyzer module operated using Nova software.

When performing EIS at different potentials, the potential is altered in steps of 100 mV starting from OCV. After every step the current is allowed to relax until a steady state is reached before an impedance measurement is performed. From the relaxation measurements the total charge flowing into the layer was calculated. The fitting of the impedance data was done using the MEISP software (Kumho Chemical Laboratories). The

Table 1 Stoichiometry of the different $Li_xMg_{1-2x}Al_{2+x}O_4$ films as determined by ERD and RBS. The value between brackets corresponds to the atomic percentage based on the target stoichiometry. The deposited films are somewhat rich in aluminum and poor in magnesium and lithium. This is likely due to the preferential sputtering of Al from the stoichiometric target

Target composition	Techn.	Li (%)	Mg (%)	Al (%)	O (%)
$MgAl_2O_4$ as-deposited	RBS	—	29.4 (33)	70 (66)	—
$Li_{0.05}Mg_{0.9}Al_{2.05}O_4$ ann.	ERD	0.48 (0.7)	9.5 (12.8)	30 (29)	60 (57.1)
$Li_{0.15}Mg_{0.7}Al_{2.15}O_4$ ann.	ERD	1.4 (2.1)	6.4 (10)	35 (30.7)	57.2 (57.1)
$Li_{0.25}Mg_{0.5}Al_{2.25}O_4$ ann.	ERD	2.5 (3.6)	4.7 (7.1)	33.3 (32)	59 (57.1)

29046 | *Phys. Chem. Chem. Phys.*, 2015, **17**, 29045–29056

This journal is © the Owner Societies 2015

obtained fits have a χ^2 in the range 10^{-3} to 10^{-4}, indicating a reliable fit. The relative standard deviation of the fitted values is approximately 10^{-3} or lower.

To conduct electrical measurements, gold metal dots (blocking contacts) were evaporated on the layers through a shadow mask. Both current–voltage (*I–V*) and impedance characterization were performed: the *I–V* measurements were carried out using an Agilent 4156C precision semiconductor parameter analyzer.

Results and discussion

Physical characterization

Fig. 1 shows the results of XRD characterization of 100 nm thick $Li_xMg_{1-2x}Al_{2+x}O_4$ (*x* between 0 and 0.25) layers, sputtered on a platinum current collector. It can be seen that all the layers exhibit the spinel structure (space group $Fd\bar{3}m$). The crystal planes are indicated according to JPDS entry 01-072-6950. Substrate contributions are also visible next to the $Li_xMg_{1-2x}Al_{2+x}O_4$ peaks, that is, peaks due to the Pt current collector and the TiO_2 (rutile) adhesion layer which are labeled on the XRD pattern. No impurity phases were detected in these patterns.

From the width of the (111) peak in the XRD pattern, the lattice constant was calculated and is plotted *versus* the layer stoichiometry in Fig. 1b. The values obtained by modeling[25] and powder diffraction[8] are shown for comparison. Similar values and trends are found in all cases, thus confirming the formation of spinel structured $Li_xMg_{1-2x}Al_{2+x}O_4$ thin films. The slight off-set of the simulated data points is within expectation as explained elsewhere.[25] The linear relationship between the lattice parameters and lithium content indicates a solid solution behavior between $MgAl_2O_4$ (a = 8.08 Å[30]) and $LiAl_5O_8$ (a = 7.903 Å[31]), in accordance with Vegard's law.[32]

The stoichiometry of the layers was probed by RBS and ERD (see Table 1). The latter was used to determine the lithium content of the layers. The experiments show that the crystalline layers are slightly lithium and magnesium deficient, and aluminum enriched. The stoichiometry for the as-deposited and annealed samples was comparable (see also Table S1 in the ESI†), except for a slight decrease in the oxygen content after

annealing. This is a known problem in materials requiring a high temperature annealing process.[33]

The excess aluminum and deficiency in Mg and Li in the studied layers is attributed to preferential sputtering of aluminum. This is a common problem when sputtering from a stoichiometric, multi-element target.[34] Upon annealing in an oxygen atmosphere at a temperature of 900 °C, *i.e.* higher than the 800 °C applied here, for 12 h the formation of Al_2O_3 or $LiAl_5O_8$ has been discovered in powder systems.[8] Both of these compounds have a higher atomic percentage of aluminum compared to $Li_xMg_{1-2x}Al_{2+x}O_4$. In the current work, no peaks of Al_2O_3 or $LiAl_5O_8$ are detected by XRD (*cf.* Fig. 1); the spinel phase is obtained with the expected lattice parameters. However, the presence of some amorphous Al_2O_3 cannot be excluded, as the annealing temperature used here (800 °C) is too low to obtain crystalline Al_2O_3.[35]

$LiAl_5O_8$ is an inverse spinel with lattice constants very close to the $MgAl_2O_4$ spinel, therefore both have closely related XRD patterns. This makes identification of the different materials very difficult. Most likely no $LiAl_5O_8$ is present in the layers sputtered here, a conclusion based on the observed linear trend in the lattice parameter and the comparison of the intensity pattern of the different stoichiometries. Again, the existence of the amorphous phase cannot be excluded. If occurring, the presence of both Al_2O_3 or $LiAl_5O_8$ will obviously impact the ionic conductivity of the material.

The morphology of the $Li_xMg_{1-2x}Al_{2+x}O_4$ layers was investigated using a combination of TEM and SEM. Fig. 2a shows an SEM image of an unannealed $MgAl_2O_4$ layer. A smooth layer can be seen on top of the platinum current collector. The lack of fine structure within the layer confirms its amorphous character as seen in the inset of Fig. 2a. Fig. 2b shows a $Li_{0.05}Mg_{0.9}Al_{2.05}O_4$ layer on top of a platinum current collector layer after crystallization annealing at 800 °C. The layer is closed and pinhole free. The polycrystalline nature of the layer can be ascertained from the granular morphology that can be clearly distinguished in the inset. An increased crystal size is also seen within the platinum layer after annealing. Note that the film forms a close contact with the underlying current collector, thus ensuring good electrical contact.
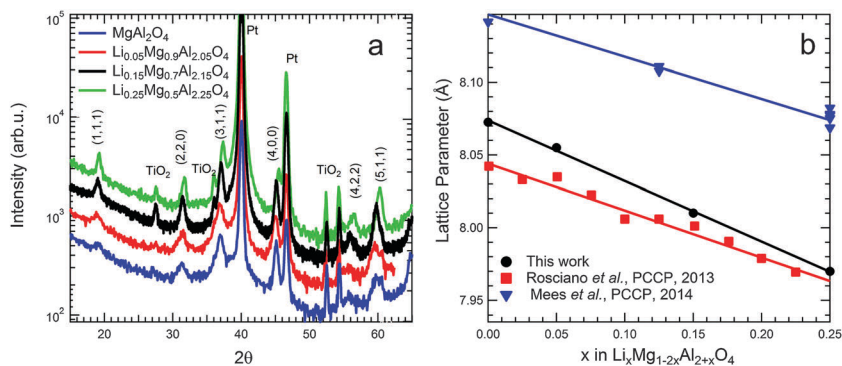

Fig. 1 (a) XRD pattern of 100 nm thick layers of $Li_xMg_{1-2x}Al_{2+x}O_4$ with different stoichiometries. All layers crystallize in the spinel phase after annealing at 800 °C for 1 h. An offset was applied to the different patterns for clarity. Clear peaks characterizing the spinel phase can be seen, the different crystal planes are indicated. (b) shows the variation of the lattice parameter as a function of the Li content of the layers. The trend fits well with results based on powder samples and modeling.[8,18,25]
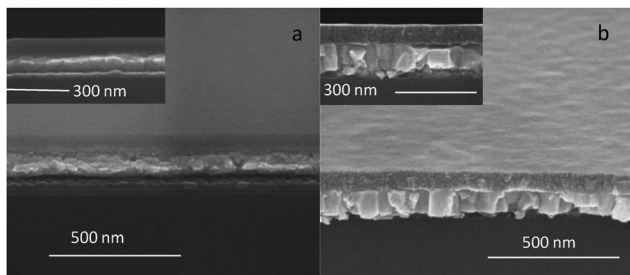
This journal is © the Owner Societies 2015

Phys. Chem. Chem. Phys., 2015, **17**, 29045–29056 | **29047**

Fig. 2 (a) SEM image of a 70 nm thick as-deposited $MgAl_2O_4$ layer on a platinum current collector exposing a smooth closed film. The inset is a cross-sectional SEM picture showing a dense layer on the platinum current collector. (b) SEM pictures of a 75 nm thick layer of $Li_{0.05}Mg_{0.9}Al_{2.05}O_4$. A smooth, closed layer is visible after annealing at 800 °C. No holes or cracks are detected. There is a close contact between the platinum current collector and the electrolyte layer. The inset showed a higher magnification of the layer making the granular nature more clearly visible.

TEM characterization was performed on crystalline 150 nm films of $Li_{0.25}Mg_{0.5}Al_{2.25}O_4$. Fig. 3 shows the key results of this characterization, more detail is provided in the ESI† (Fig. S1 and S2). It is known that with increasing lithium content, phase separation into $MgAl_2O_4$ and amorphous $LiAl_5O_8$ is more likely, as concluded from first principles simulations.[25] However, the $Li_{0.25}Mg_{0.5}Al_{2.25}O_4$ film, having the highest lithium stoichiometry investigated here, remains highly crystalline, as illustrated in Fig. 3a. The spinel crystal lattice can be seen in all regions of the image. From the high resolution TEM fast Fourier transform a lattice constant of 8 Å is found, in good agreement with the value inferred from the XRD data shown in Fig. 1.
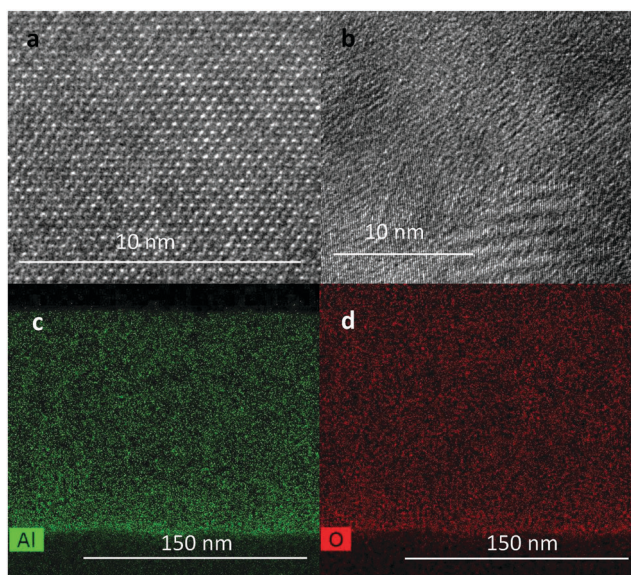

Fig. 3 (a) TEM image of a 150 nm thick highly crystalline $Li_{0.25}Mg_{0.5}Al_{2.25}O_4$ layer. The atomic lattice can be clearly distinguished. (b) shows a TEM image of the same layer but at a different place in the sample. The lattice can again be clearly seen indicating the highly crystalline nature of the material after annealing. Near the bottom of the layer, twinning is observed. (c and d) show the results of the TEM-EDS analysis. No local increases in aluminum or oxygen are detected; all of the elements are evenly distributed throughout the material.

Fig. 3b is an image taken at a different area of the sample than pictured in a, exposing differences in contrast. This dissimilarity can be due to the different grain orientation in the sample but could also be the result of the presence of amorphous material. Yet, we note that even in the areas where the contrast difference is present, the layer remains crystalline. Therefore if the change would be due to the presence of an amorphous region in the material it never spans the entire thickness of the TEM lamella (50 to 70 nm). Towards the bottom of the image typical twinning is observed; the twins also show distinct contrast in the image, reinforcing the idea that these contrast differences originate from different grain orientations.

To assess the possibility of phase separation into amorphous Al_2O_3 or $LiAl_5O_8$ constituents, TEM coupled energy-dispersive X-ray spectroscopy (EDS) was conducted. The aluminum and oxygen images are shown in Fig. 3c and d respectively. No local aluminum or oxygen enrichment could be detected. Also, no direct correlation was found between the observed contrast differences and the elemental distribution. All the investigated elements (Al, O) are found to be evenly distributed over the layer. Note that no magnesium map is shown since the Mg signal overlaps with the platinum of the current collector.

From the physical characterization data outlined above, it can be concluded that polycrystalline $Li_xMg_{1-2x}Al_{2+x}O_4$ films were fabricated, hereafter referred to as crystalline films for the sake of brevity. These are slightly lithium and magnesium deficient, and aluminum rich. The material crystallizes in the spinel crystal structure after annealing at 800 °C for 1 h in an oxygen atmosphere.

Electrical and electrochemical characterization

The sputtered $Li_xMg_{1-2x}Al_{2+x}O_4$ films were also evaluated for their solid electrolyte properties. Independent NMR measurements on $Li_xMg_{1-2x}Al_{2+x}O_4$ powders indicated an activation energy for ionic conductivity as low as 0.35 eV for $x = 0.05$.[8] For this reason good ionic conductivity is anticipated in similar layers. Furthermore, the material is known to have a wide electrochemical window (between 0 and 10 V vs. Li^+/Li).[8] The electronic conductivity of the material is expected to be low due to its wide bandgap.[25]

The electronic leakage was investigated first using metal–insulator–metal (MIM) capacitors fabricated using thermally evaporated gold dots. Fig. 4 displays the I–V characteristics for 100 nm crystalline layers of $Li_xMg_{1-2x}Al_{2+x}O_4$ with x between 0 and 0.25. The leakage current density remains below 45 nA cm^{-2} over the whole voltage range probed. This low leakage confirms the absence of cracks and pinholes, as assessed from the SEM images in Fig. 2. Because of the use of two blocking contacts (Pt and Au), only a limited contribution of the mobile lithium ions is expected.

At 2 V an average current density of 2×10^{-8} A cm^{-2} is measured for the different layers, corresponding to a resistivity of 10^{13} Ω cm. This is in the same range as what has been reported for Al_2O_3 elsewhere,[36,37] indicating negligible contribution of the mobile ions in the layers. The obtained response is similar to
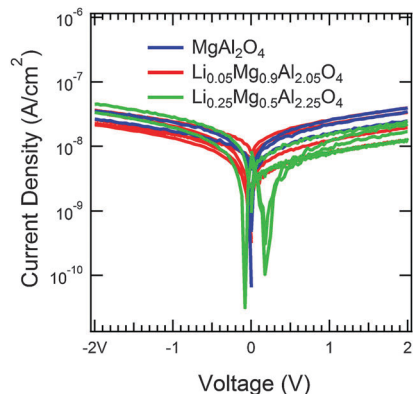
29048 | *Phys. Chem. Chem. Phys.*, 2015, **17**, 29045–29056

This journal is © the Owner Societies 2015

Fig. 4 *I–V* data of a 100 nm thick crystalline $Li_xMg_{1-2x}Al_{2+x}O_4$ (x in the range of 0 to 0.25) film using gold blocking electrodes. The current density remains low throughout the whole voltage range probed. This proves the absence of pinholes and the insulating properties of the investigated layers.

typical good dielectrics such as SiO_2 and Al_2O_3. It confirms the good dielectric properties of the $Li_xMg_{1-2x}Al_{2+x}O_4$ layers.

The results of the *I–V* measurements on the amorphous $Li_xMg_{1-2x}Al_{2+x}O_4$ layers are depicted in the ESI† (Fig. S3). Leakage current density of these layers is roughly an order of magnitude smaller than for the crystalline layers.

The high resistivity proves the insulating character of the material, an inherent advantage of a $MgAl_2O_4$-based electrolyte. Undoped $MgAl_2O_4$ has a bandgap of 7.8 eV and therefore a very low electronic conductivity.[38,39] Furthermore, it was concluded from first principles calculations by Mees *et al.*[25] that the bandgap remains unchanged by doping with Al and Li.

We have thus shown the electronic insulating properties of the $Li_xMg_{1-2x}Al_{2+x}O_4$ layers which are indeed required for a solid electrolyte. However, also good ionic conductivity and high stability are needed. To assess these properties, electrochemical measurements were performed.

Fig. 5a shows the observed current–potential curves for the 100 nm thick crystalline $Li_xMg_{1-2x}Al_{2+x}O_4$ layers ($x = 0$ and 0.25) on platinum as well as for a bare platinum electrode. The

material was evaluated in a potential range from −0.1 V up to 4 V *vs.* Li^+/Li. The bare platinum electrode shows clear lithium plating and stripping peaks around 0 V. Plating sets in from approximately 0.3 V on. This early onset is likely caused by underpotential deposition (UPD) on platinum; UPD deposition of lithium on platinum substrates is a known phenomenon.[40] The charge under the UPD peaks is 2.1 mC cm^{-1} corresponding to 31 monolayers of lithium. This number is too high for UPD, typically 1 or 2 monolayers. However, due to the lithium–platinum alloy formation, UPD deposition can continue for a longer time.

In the reverse scan, lithium stripping is seen when the potential is increased above 0 V. When further raising the potential to 0.3 V another set of peaks is observed, corresponding to the dealloying from the lithium–platinum alloy.[40,41] A charge of 5.6 mC cm^{-2} of lithium is plated, while only 2.2 mC cm^{-2} is stripped. This continues up to approximately 1.5 V *vs.* Li^+/Li when the remaining 3 mC cm^{-2} is extracted.[40] The peak at 1.8 V corresponds to intercalation and extraction of lithium into the TiO_2 adhesion layer. The peak at approximately 3 V is not clearly attributable.

When comparing the current–potential curves of the bare platinum with those of the $Li_xMg_{1-2x}Al_{2+x}O_4$ layers on platinum, the current of the latter is 2 to 3 orders of magnitude lower as evident from Fig. 5a. The inset illustrates that the current remains low in the potential range from 0.3 to 4 V *vs.* Li^+/Li, the value remaining around 10^{-7} A cm^{-2}. This confirms the stability of the electrolyte in this window.

Upon decreasing the potential below 0.3 V, an increase in current is seen. This increase in current is attributed to the onset of Li plating through the $Li_xMg_{1-2x}Al_{2+x}O_4$ layer, a result of the onset of UPD on Pt as observed for the platinum reference. As for the bare platinum a steep increase in current is seen when the potential drops below 0 V, corresponding to the onset of Li-plating on the platinum substrate under the $Li_xMg_{1-2x}Al_{2+x}O_4$ film and likely Li–Pt alloy formation.

Upon reversing the potential, the Li-ions are stripped again. The clear similarity between the platinum reference and the
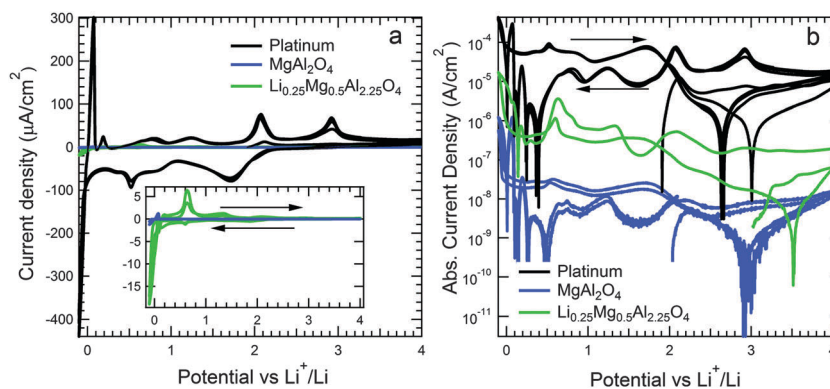

Fig. 5 (a) Cyclic voltammograms of 100 nm thick crystalline $Li_xMg_{1-2x}Al_{2+x}O_4$ layers and a platinum reference. The layer can be seen to be stable in a voltage range from 0.3 up to 4 V *vs.* Li^+/Li. The inset shows only the $MgAl_2O_4$ and $Li_{0.25}Mg_{0.5}Al_{2.25}O_4$ current potential traces. (b) shows the current potential curves plotted on a logarithmic scale. This reveals the presence of several smaller peaks in the $Li_xMg_{1-2x}Al_{2+x}O_4$ layers corresponding to lithium–platinum alloy formation.

$Li_xMg_{1-2x}Al_{2+x}O_4$ layers hints at the formation of similar alloys. Since the $Li_xMg_{1-2x}Al_{2+x}O_4$ layers are electronically insulating, as was shown above, lithium ions must be transported through the layers. Only upon reaching the platinum current collector, reduction to metallic lithium and platinum–lithium alloy formation can occur.

Fig. 5b depicts the current–potential curves shown in Fig. 5a on a logarithmic scale. In the reverse scan, stripping of the lithium is seen from 0 V onward, with a distinct current peak in all cases. However, all cathodic charge is extracted again only when increasing the potential to 1.5 V. This is explained by the formation of lithium–platinum alloys also for the cases with $Li_xMg_{1-2x}Al_{2+x}O_4$ layers. The distinct Li–Pt alloy peaks are clearly revealed in Fig. 5b. Peaks are present around 0.2, 0.5 and 1.2 V. These match with those seen for the bare platinum reference layer. The appearance of these (de)alloying peaks confirms the ability of lithium transport through the $Li_xMg_{1-2x}Al_{2+x}O_4$ layers.

To determine the ionic conductivity, EIS was performed. First we will discuss the results obtained at OCV; in later paragraphs we will discuss the potential dependence of the impedance response.

EIS observations on 100 nm thick crystalline $Li_xMg_{1-2x}Al_{2+x}O_4$ films, performed at OCV, are depicted in Fig. 6 on a complex plane or Nyquist plot. Ionic conductivity is typically characterized by the presence of a semi-circle. The first intercept of this circle with the real axis corresponds to the series resistance (generally attributed to cables, contacts and the liquid electrolyte), the second one to the ionic resistance of the solid electrolyte.[42] Fig. 6 shows the results measured on $Li_xMg_{1-2x}Al_{2+x}O_4$ ($x = 0$ to 0.25) layers.

No clear semi-circle can be detected for the $Li_xMg_{1-2x}Al_{2+x}O_4$ layers with $x = 0$, 0.05 and 0.15. Only the $Li_{0.25}Mg_{0.5}Al_{2.25}O_4$ layer shows a large semi-circle (intercepting the real axis at 2 MΩ), corresponding to an ionic conductivity of approximately 1×10^{-11} S cm^{-1}. This low conductivity limits practical applicability and differs from the conductivities anticipated elsewhere.[8,18]

The conductivity behavior of the $Li_xMg_{1-2x}Al_{2+x}O_4$ layers (with $x = 0$, 0.05 and 0.15) closely resembles an ionic blocking layer. This contrasts with the findings by NMR, where the layer with $x = 0.05$ showed the clearest signature of conductivity. The absence of ionic conductivity as reflected by the EIS data indicates that the NMR line width measurements likely determined Li hopping between the 8a and 16c spinel crystal positions.[8] This hopping does not necessarily result in long range lithium ion conductivity as the Li-ion can go back and forth between 8a and 16c positions. Mees *et al.* concluded that the lowest energy path for Li-ion diffusion would be from 8a to 16c and then into the next neighboring 8a site. The 16c site thus emerges as an intermediate position in ionic motion.[25]

Potential dependent conductivity

The poor conductivity found from the impedance measurements seems contradictory to the fact that lithiation is observed in the cyclic voltammetry data. Indeed, the presence of lithium–platinum alloy formation and lithium plating illustrates the possibility of conductivity through the $Li_xMg_{1-2x}Al_{2+x}O_4$ layers. Various reasons for this discrepancy can be thought of, *e.g.*, lithium transport through grain boundaries on application of an electric field, liquid electrolyte penetrating into defects or lithiation of the $Li_xMg_{1-2x}Al_{2+x}O_4$ layers in a mechanism similar to Al_2O_3.[43] The mechanism of the lithium transport will be investigated in the following paragraphs.

To assess the effect of grain boundaries, amorphous (*i.e.*, not annealed) $Li_xMg_{1-2x}Al_{2+x}O_4$ layers have been subjected to cyclic voltammetry experiments (data shown in ESI,† Fig. S4). For these amorphous layers, cyclic voltammetry still showed distinct lithium plating peaks and lithium–platinum alloy formation, confirming ionic movement through the layer. The currents are in the same order of magnitude as those of the crystalline $MgAl_2O_4$, leading to the conclusion that grain boundary transport is not the main facilitator of ionic conductivity through the layers.

To assess the possibility of pinholes in the films, copper plating and stripping experiments were conducted. SEM inspection showed no obvious presence of defects or pinholes in the films (*cf.* Fig. 2). Also electrical characterization (Fig. 4) did not reveal any shorting. However, SEM cannot detect the small pinholes and the evaporated metal dots might not contact them. In the wet copper plating and stripping experiments, the aqueous solution will be able to access even the smallest pinholes.[44] On the other hand it is assumed that the doubly charged copper ion will not be transported through the $Li_xMg_{1-2x}Al_{2+x}O_4$ layer.

Copper plating and stripping measurements using cyclic voltammetry on $MgAl_2O_4$ coated platinum substrates did show evidence of copper plating and stripping (see Fig. S5 in the ESI†). However, the measured plating currents are in the same order of magnitude as the electronic leakage through the dielectric films (see Fig. 4). Therefore, it is likely that copper is initially plated due to the electronic leakage. This plated copper can introduce further defects in the $MgAl_2O_4$ layers.

Coincidently, the plating currents observed on amorphous $MgAl_2O_4$ are 100 times smaller than for the crystalline films, as is approximately also the case for the leakage currents. Additionally, a large IR drop is found for the copper plating and stripping in both annealed and unannealed $MgAl_2O_4$
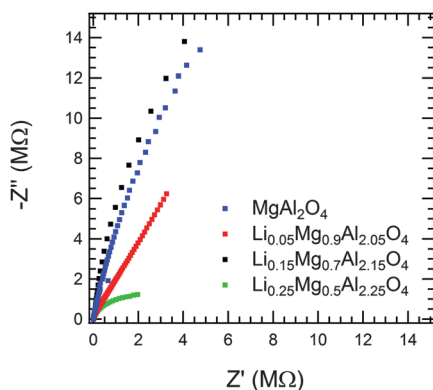

Fig. 6 Nyquist plots of different $Li_xMg_{1-2x}Al_{2+x}O_4$ layers measured at OCV. No clear conductivity signature is detected for the layers with stoichiometry from $x = 0$ to 0.15. $Li_{0.25}Mg_{0.5}Al_{2.25}O_4$ shows a large semi circle, intercepting the real axis at 2 MΩ.

29050 | *Phys. Chem. Chem. Phys.*, 2015, **17**, 29045–29056

This journal is © the Owner Societies 2015

layers, indicating their good electronically insulating quality. However, we cannot fully exclude that there is some contribution of grain boundaries and defects in the annealed layers. The effect of these should however remain limited as similar lithium plating and stripping currents are seen in the amorphous and crystalline $Li_xMg_{1-2x}Al_{2+x}O_4$ layers.

To further investigate the transport of lithium through the $Li_xMg_{1-2x}Al_{2+x}O_4$ layers, EIS measurements were performed at various potentials. The potential was lowered from OCV (around 3 V vs. Li^+/Li) down to 0.1 V in steps of 100 mV. The lower cutoff potential was limited to 0.1 V to prevent delamination of the $Li_xMg_{1-2x}Al_{2+x}O_4$ layer from the platinum current collector. This due to lithium plating at the interface between the latter two layers during the long measurement times.

After every potential step, the current was allowed to relax until a steady state was reached, which was then followed by an impedance spectroscopy measurement (see ESI,† Fig. S6). The frequency spectrum obtained this way was fitted using the circuit shown in Fig. 7. A detailed element assignment is given at a later stage. Fig. 8 shows an overview of the impedance behavior for a 100 nm thick amorphous $MgAl_2O_4$ layer. Fig. 8a presents a logarithmically scaled complex plane plot of the data obtained at different potentials (starting at OCV) – this for easy comparison of values and features as the response profoundly changes with decreasing potential. The full line is the fit through the data points based on the model of Fig. 7, indicating that the model used fits the changing impedance response well.[42]

Fig. 8b shows a complex plane plot zoomed-in on the high frequency region. A good fit of the model to the data can be seen over the entire potential range. Generally, the χ^2 square values range between 10^{-3} and 10^{-4}, indicating a reliable fit.[45] This confirms the suitability of the model to analyze the acquired impedance data. The layer response changes from that characteristic for a capacitor at high potentials, which is seen almost as a vertical line, to a semi-circle. The semi circle seen at lower potentials is commonly modeled by a resistor in parallel with a capacitor. When measuring solid electrolytes, such response is commonly attributed to the electrostatic capacitance of the layer and the resistance of Li-ion transport through the layer.

Fig. 8c and d show the variation of the resistance values as extracted from the impedance data. These resistances, R_1 and R_2, correspond to the components shown in Fig. 7. Fig. 8c shows the changes in resistances and the charge that flows when decreasing the potential from OCV to 0.1 V vs. Li^+/Li. This charge is calculated by integrating the current that flows during the 1 h relaxation time (see the figure in the ESI†) after every

discrete potential step. All the data shown here are calculated for steps of 0.1 V. Fig. 8d depicts the behavior of these elements (R_1, R_1 and the charge that flowed during every discrete step) upon increasing the potential back to OCV. The left axis on the figures corresponds to the resistance values, and the right axis shows the absolute charge that flowed during every potential step. From these figures a complete picture of the variation in resistance of the layer with changing potential is obtained.

Upon lowering the potential, a plateau is visible in the resistance values (see Fig. 8c). This persists from 3 V to approximately 0.6 V vs. Li^+/Li. When the potential drops below 0.6 V a reduction in resistance is measured, coinciding with an increased charge flow. Eventually, a drop in resistance (R_2) of over 3 orders of magnitude from the plateau value is achieved at a potential of 0.1 V. This is also reflected in the abrupt change of the impedance response in Fig. 8a and b. Upon increasing the potential again, the resistances evolve back to their original state, but only when a potential of approximately 2 V is reached. Hence a hysteresis of ~1 V is present when comparing the down and up traces, cf. Fig. 8c and d, respectively.

A similar trend is observed in the measured charge associated with each discrete potential step. From 3 V up to 0.6 V versus Li^+/Li negligible charge flows, following the plateau trend seen in the resistance. Starting from 0.6 V, an increased (negative) charge flow is seen in Fig. 8c, which increases steeply. During the reverse cycle (cf. Fig. 8d), increasing the potential again, a large (positive) charge flow now exists up to approximately 1.5 V, after which it reduces to the background level. A clear charge peak is seen around 0.6 V vs. Li^+/Li. In the cyclic voltammogram of Fig. 5 a peak was found at this potential as well which was attributed to a lithium–platinum dealloying peak. Thereby the behavior of the charge closely resembles the current–potential curves of Fig. 5.

A clear hysteresis is present when comparing the measured evolution of the resistance and charge for decreasing or increasing potential (cf. comparing panels c and d in Fig. 8). The original resistance values are only recovered upon reaching a potential of 1.5 V, coinciding with the final lithium–platinum dealloying peak. Both the charge shown in Fig. 8c and d and the cyclic voltammogram of Fig. 5 show peaks at 0.5 V and 1.5 V vs. Li^+/Li attributed to the (de)alloying from platinum.

The influence of the platinum current collector is confirmed by performing similar experiments on a TiN current collector. When amorphous $Li_{0.25}Mg_{0.5}Al_{2.25}O_4$ is deposited hereon, the initial resistance values are regained in reverse trace at 1 V vs. Li^+/Li (1 V faster than on Pt) (see Fig. S8 in the ESI†), reflecting a more symmetric behavior. The lithium–platinum alloy formation as a cause for the hysteresis in these experiments is hereby established. From this it can be concluded that the charging current, seen in Fig. 8, is due to the movement of lithium ions through or into the $Li_xMg_{1-2x}Al_{2+x}O_4$ layer and subsequently in the platinum current collector.

As the charge that flows upon a potential step is due to a Li-ion current, the entry of Li-ions into the layer causes the reduction in resistance. Such a decrease only occurs provided
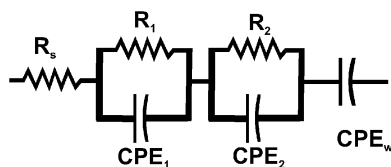

Fig. 7 Equivalent circuit model used to fit the impedance data obtained by performing impedance spectroscopy at varying potential values.
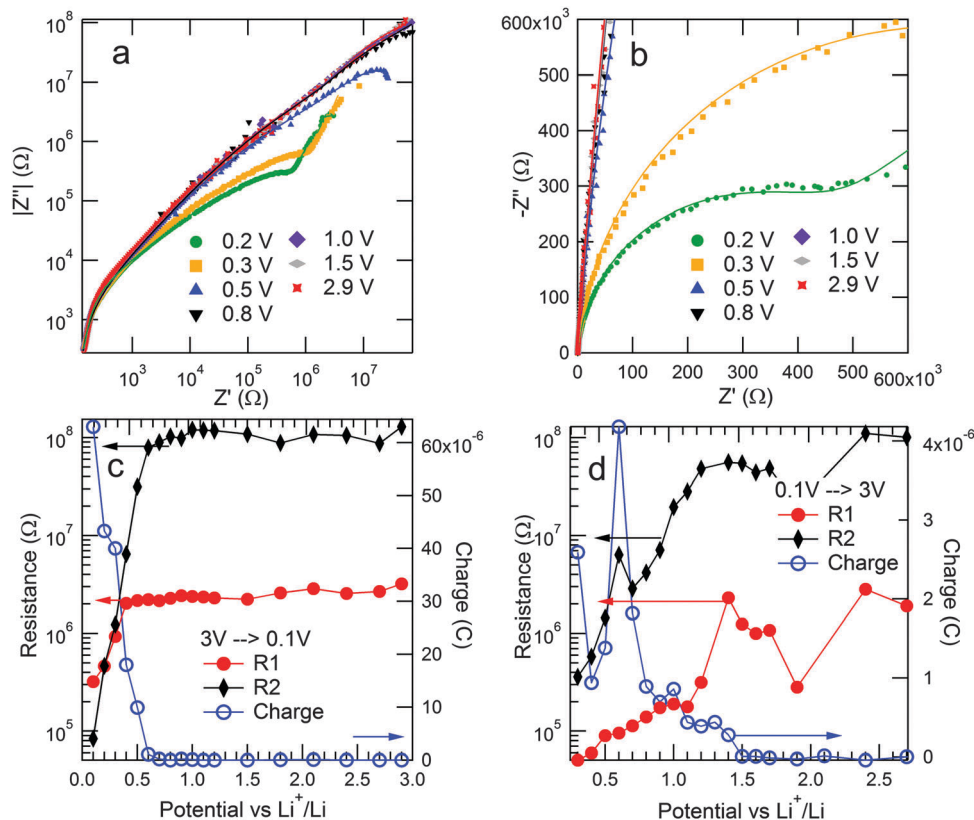
Fig. 8 (a) Logarithmically scaled complex plane plot of the variation in impedance characteristics of a 100 nm thick unannealed $MgAl_2O_4$ layer at different potentials. The solid line represents the fit to the data based on the equivalent circuit model depicted in Fig. 7. (b) Complex plane plot showing the high frequency region of the data. Also in this case the model is found to fit the data well. (c and d) Overview of the variation in model parameters of a 100 nm amorphous $MgAl_2O_4$ layer upon lowering (c) and increasing the potential (d). A drop in resistance of over 3 orders of magnitude is seen upon lowering of the potential. Upon increasing the potential a hysteresis is visible, attributable to the platinum current collector acting as a source of lithium.

the inserted lithium ions are mobile. Note that we started from a lithium free $MgAl_2O_4$, so the introduction of lithium ions, thus an increase in Li^+ concentration, would indeed lower the resistance. At its optimum, the total conductivity of the $MgAl_2O_4$ layer shown here reaches 10^{-10} S cm^{-1}. Upon increasing the potential again, the lithium ions move out of the layer and the resistance returns to its original value. Since lithium dealloys from the platinum current collector up to 1.5 V, it acts as a source of lithium.[40,41] The platinum–lithium alloy supplies Li-ions into the layer which keeps the resistance low. Once the platinum has completely dealloyed, the lithium is removed from the layer and the resistances evolve to their initial value.

From Fig. 8, one might feel tempted that the resistance reduction is linked to the change in DC current. However this is not the case. The resistance is measured at the end of the 1 h current relaxation or equilibration step and the current after such a step shows minor dependence on the potential (see ESI,† Fig. S7). The limited change in current can therefore not account for the observed change of over 3 orders of magnitude in the impedance response.

The behavior described above regarding the impedance characteristics was found in $MgAl_2O_4$ and $Li_{0.25}Mg_{0.5}Al_{2.25}O_4$ layers with various thicknesses, both in the amorphous and crystalline state. All of these layers showed a behavior similar to the one depicted in Fig. 8.

Conductivity mechanism

The entry of positively charged lithium ions into the $Li_xMg_{1-2x}Al_{2+x}O_4$ layer leads to a charging of the material. A fraction of this charge can be of a capacitive nature, *e.g.*, formation of the double layer. However the magnitude of the charge measured here cannot solely be explained by the formation of a double layer. The accumulated charge at 0.1 V is approximately 0.3 mC cm^{-2} and corresponds to approximately 4–5 nm plated lithium; such charge is too large to be accounted for by the formation of a double layer (typically in the μC range).[46] Furthermore, the growth of an electrochemical double layer can also not explain the drop with a factor of 10^3 in the resistance.

It is thus more likely that a reaction occurs involving the $Li_xMg_{1-2x}Al_{2+x}O_4$ layer and the lithium ions, similar to electrode intercalation. Lithiation of Al_2O_3 has been shown before.[43,47] It was reported that metallic lithium reacts with the Al_2O_3 until a composition of $Li_{3.4}Al_2O_3$ is formed. This composition is thermodynamically the most favorable and has a Li-ion conductivity 3 orders of magnitude larger than $Li_xAl_2O_3$ with compositions

29052 | *Phys. Chem. Chem. Phys.*, 2015, **17**, 29045–29056

This journal is © the Owner Societies 2015

between x = 0.2 and 0.4.[43] Note that in this compound the oxidation state of Al has changed from (+III) to (+II).

A similar mechanism seems to be operating in the layers studied in this work. Gradual lithiation of the $Li_xMg_{1-2x}Al_{2+x}O_4$ leads to an increased lithium ion conductivity, the lithiation proceeds until a stable composition is formed that shows a significantly higher conductivity (roughly an increase of 3 orders of magnitude). The Li^+-ion intercalation reaction may then be described by the equation:

$$MgAl_2O_4 + xe^- + xLi^+ \leftrightarrow Li_xMgAl_2O_4 \qquad (1)$$

Reaction (1) shows that the insertion of lithium ions in the layer coincides with a reduction of the aluminum's oxidation state from (+III) to (+II) thus ensuring charge neutrality as for Li^+-ion intercalation electrodes. The reaction will proceed until the thermodynamically most favorable composition is obtained as reported for Al_2O_3.[43] Once this composition is formed, which has a higher Li-ion conductivity, the material functions as an ionic conductor and facilitates lithiation of the platinum current collector. The indifference of the mechanism proposed here to the starting stoichiometry and annealing condition of the studied layers matches well with the observations.

Note that $Li_xMgAl_{2+x}O_4$ which forms in reaction (1) differs from the original material. In the sputtered $Li_xMg_{1-2x}Al_{2+x}O_4$ the oxidation state of the aluminum remains fixed at (+III), independent of the lithium content. However, when lithium is electrochemically intercalated the aluminum has to change the oxidation state to preserve charge neutrality.

Different reasons can now be suggested for the reduction of the resistance. First, the lowering of the resistance seen in the $Li_xMg_{1-2x}Al_{2+x}O_4$ layers could be due to the lithiation of Al_2O_3 present in the layers. However, similar reductions in resistance are seen in crystalline and amorphous $Li_xMg_{1-2x}Al_{2+x}O_4$ while no Al_2O_3 is present in the amorphous material. Furthermore, from Fig. S9 in the ESI,† it is seen that the lithiation of Al_2O_3 is an irreversible process. Once the low resistance state is reached, the original layer resistance cannot be recovered, whereas by contrast, the variations in resistance of $Li_xMg_{1-2x}Al_{2+x}O_4$ are shown to be reversible.

The results reported here (cf. Fig. 9 and ESI,† Fig. S9) are in good agreement with the modeling results reported elsewhere.[43] They also constitute the first experimental investigation of the changing ionic conductivity of buffer layers both $Li_xMg_{1-2x}Al_{2+x}O_4$ as well as for Al_2O_3.

Another explanation for the drop of resistance might originate from the change in electronic conductivity on intercalating Li in the $Li_xMg_{1-2x}Al_{2+x}O_4$. The oxidation state of aluminum changes during reaction (1), and the mixed valence state will lead to a higher electronic conductivity. However, in this case no influence would be expected from the platinum current collector. No difference would be present between the
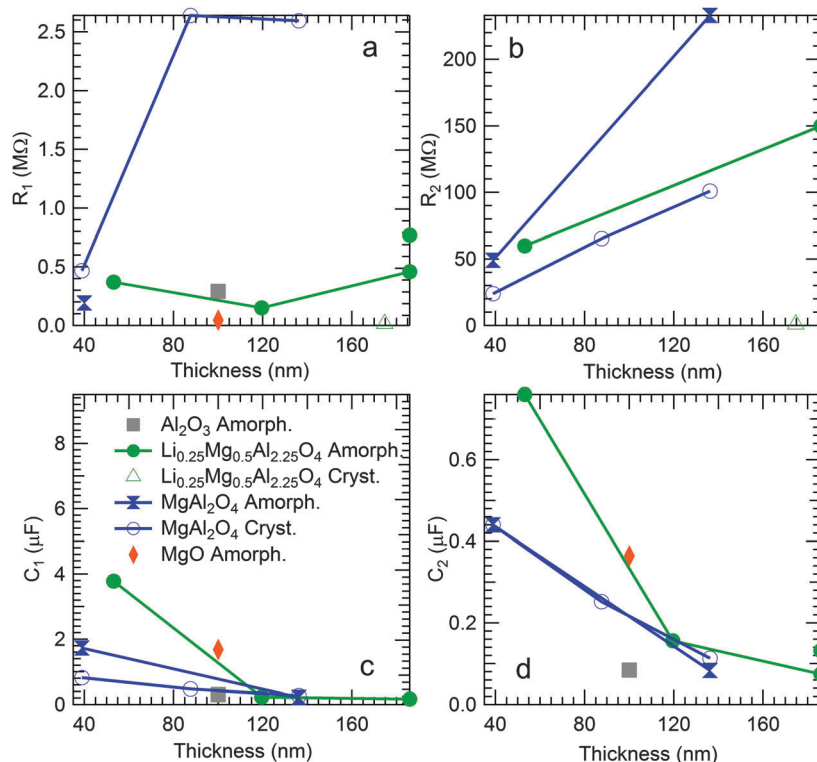

Fig. 9 (a) depicts the changes of R_1, determined from the plateau (3–1 V vs. Li^+/Li) data (cf. Fig. 8c and d), versus the layer thickness. Little variation is seen with varying layer thickness. (b) shows the variation of R_2 versus layer thickness. A linear relationship between the two quantities is seen. (c) shows the capacity extracted from CPE_1, (cf. Fig. 7), versus layer thickness. Only a limited variation is seen in the C_1 value when changing the layer thickness. (d) depicts the variation of C_2 (extracted from CPE_2). As the layer thickness decreases C_2 increases, as is expected for a capacitor.

measurement on a TiN or Pt substrate, while clear differences are shown here. The platinum substrate leads to a hysteresis, delaying the recovery of the original resistance values. This phenomenon was explained by the platinum–lithium alloy acting as a source of lithium for the $Li_xMg_{1-2x}Al_{2+x}O_4$ layer. The changing resistance can thus be attributed to the presence of lithium in the $Li_xMg_{1-2x}Al_{2+x}O_4$ layer, and hence the observed changes in resistance are concluded to correspond to a change in the ionic conductivity of the material.

From the above it is thus concluded that $Li_xMg_{1-2x}Al_{2+x}O_4$ does not function as a solid electrolyte. Instead it intercalates lithium at low potentials and thus operates as an electrode with low electronic conductivity. For this reason $Li_xMg_{1-2x}Al_{2+x}O_4$ could be used as a buffer layer similar to Al_2O_3 for lithium ion electrodes.[48,49] The recovery of the original resistance state after the experiment hints at good reversibility of the process, however more detailed cycling experiments are needed to confirm these findings.

Model interpretation

As was mentioned before, all impedance data were fitted based on the circuit shown in Fig. 7. In this section the components of the model are discussed in more detail. Some of these have a straightforward meaning, others require a more in depth analysis.

The simplest element in the circuit is the series resistance R_s, commonly attributed to contact resistances, cabling *etc.* In this work its value is consistently found to be $\sim 150\ \Omega$. The CPE_W element is attributed to the low frequency diffusion component in the electrolyte. Its n value (see eqn (2)) is commonly found around 0.5 corresponding to a Warburg impedance element.

To gain insight into the meaning of the remaining elements, an overview of their plateau (3–1 V *vs.* Li^+/Li) values (*cf.* Fig. 8c and d) is presented in Fig. 9 for the different $Li_xMg_{1-2x}Al_{2+x}O_4$ layers studied.

Fig. 9a and b show the variation of, respectively, R_1 and R_2 *versus* the layer thickness. Resistance R_1 remains approximately constant upon varying the film thickness; with the exception of the 40 nm crystalline $MgAl_2O_4$ layer. R_2 on the contrary shows a linear increase with film thickness, as expected for a resistor. As shown before, R_2 is roughly two orders of magnitude larger than R_1. Both resistances do not show a clear dependence on the material stoichiometry, yet, the magnitude of R_2 for the crystalline films is consistently lower than for the amorphous ones.

Fig. 9c and d depict the variation of the capacitances associated with the constant phase elements *versus* layer thicknesses. The constant phase elements are modeled according to:[50]

$$Z_{CPE} = \frac{1}{Q_0 \omega^n} \exp^{\frac{-\pi}{2} nj} \qquad (2)$$

In this equation Z_{CPE} is the impedance of the CPE, j is the imaginary unit, Q is a fitting parameter, n is an integer (between 0 and 1) and ω equals $2\pi f$. As n varies between zero and one, the CPE response evolves from a pure resistor to a perfect capacitor. Therefore it is well suited to account for possible imperfections in the capacitors. The values found for the elements CPE_1 and

CPE_2 are assumed to be equal to the associated capacitance, *i.e.*, C_1 and C_2, respectively. This might introduce a small error, however since the n values found here are larger than 0.9, this error should remain limited. Since detailed capacitance analysis is outside the scope of this work no in depth CPE analysis has been performed.[50]

The obtained capacitance values are situated in the microfarad range for C_1 and around ten to one hundred nF for C_2. C_2 clearly depends on the layer thickness, showing an inverse relation to the layer thickness, as one would expect for a capacitance. The value of C_2, in the range of 100 of nF, fits well with typical electrostatic capacitors of, *e.g.*, Al_2O_3 (dielectric constant $\varepsilon_r \sim 7$).

C_1 on the other hand shows little dependence on the layer thickness. It shows only minor variations when changing the layer thickness. The response does not match the behavior expected for a 'classical' capacitor ($C \propto 1/d$). Its magnitude, around 10^{-6} F, matches well with typical values of an electrochemical double layer, which is expected to be independent of the layer thickness.

The behavior of the circuit elements displayed in Fig. 9 leads to the conclusion that the first RC branch (composed of C_1 (CPE_1) & R_1), represents a double layer or possibly a solid electrolyte interface. This is supported by the independence of the elements on the layer thickness and the magnitude of C_1 which matches with typical values of the electrochemical double layer.

The second RC branch corresponds to the bulk response of the material. The capacitor can be matched with the electrostatic capacitance of the layer as was shown above. The resistance values found here are attributed to the ionic conductivity of the material, which is very small in the $MgAl_2O_4$ and the unannealed $Li_{0.25}Mg_{0.5}Al_{2.25}O_4$ layer, as shown in Fig. 6. The value shown for annealed $Li_{0.25}Mg_{0.5}Al_{2.25}O_4$ in Fig. 9d matches with what was extracted from for the ionic conductivity before, namely a value of 10^{-11} S cm^{-1} (*cf.* Fig. 6).

Conclusion

The behavior of different stoichiometries of thin films of $Li_xMg_{1-2x}Al_{2+x}O_4$ ($x = 0$, 0.05, 0.15, 0.25) was evaluated as solid electrolyte. The material crystallized into the spinel structure as shown by both XRD and TEM investigations, although being aluminum rich. The layers showed low electronic conductivity, down to the thinnest layer probed here, namely 100 nm thick. This was confirmed by both dry current–voltage measurements and copper plating tests. Li-ion transport through the layers was shown by the formation of a lithium–platinum alloy in cyclic voltammetry. However, no signature of ionic conductivity was found in EIS measurements at OCV. This seeming discrepancy between the EIS investigation and cyclic voltammetry was resolved by performing potential dependent impedance spectroscopy. Such measurements showed a change of over 3 orders of magnitude in ionic conductivity upon lithium insertion into the $Li_xMg_{1-2x}Al_{2+x}O_4$ layer.

29054 | *Phys. Chem. Chem. Phys.*, 2015, **17**, 29045–29056

This journal is © the Owner Societies 2015

It was argued that the $Li_xMg_{1-2x}Al_{2+x}O_4$ layers incorporate lithium through an intercalation like mechanism. The inserted Li-ions are mobile in the layer, causing a reduction in resistance. When the thermodynamically most favorable stoichiometry is reached, Li-ions are able to cross the electrolyte and alloy with the platinum current collector. Upon increasing the potential, lithium ions are repelled from the layer. A similar mechanism has recently been demonstrated for Li-ion conductivity through Al_2O_3 which also resulted in an increase in conductivity of over 3 orders of magnitude. We have thus shown that $Li_xMg_{1-2x}Al_{2+x}O_4$ does not function as a solid electrolyte, however it might still find use as a buffer layer. In this case lattice matching can still occur between the interface of the spinel electrode (*e.g.* $LiMn_2O_4$, $Li_4Ti_5O_{12}$,...) and the buffer layer. This might lead to better performance of a lattice matched buffer layer compared to *e.g.* amorphous Al_2O_3. An additional benefit of using spinel structured buffer layers, might be an increased cyclability of the electrodes. When using spinel $Li_xMg_{1-2x}Al_{2+x}O_4$ buffer layers, the latter might provide anchoring points at the electrode interface which might help to maintain the structural integrity when these electrodes undergo volume changes or detrimental phase changes.

Acknowledgements

References

1 R. V. Noorden, *Nature*, 2014, **507**, 26–28.

2 J.-M. Tarascon and M. Armand, *Nature*, 2001, **414**, 359–367.

3 F. T. Wagner, B. Lakshmanan and M. F. Mathias, *J. Phys. Chem.*, 2010, **1**, 2204–2219.

4 A. Arico, P. Bruce, B. Scrosati, J.-M. Tarascon and W. V. Schalkwijk, *Nat. Mater.*, 2005, **4**, 366–377.

5 M. Donders, J. Oudenhoven, L. Baggetto, H. Knoops, M. V. de Sanden, W. Kessels and P. Notten, *ECS Trans.*, 2010, **32**, 213–222.

6 N. Kamaya, K. Homma, Y. Yamakawa, M. Hirayama, R. Kanno, M. Yonemura, T. Kamiyama, Y. Kato, S. Hama, K. Kawamoto and A. Mitsui, *Nat. Mater.*, 2011, **10**, 682–686.

7 P. Vereecken, 2014, http://electroiq.com/blog/2014/05/towards-all-solid-state-3d-thin-film-batteries-for-durable-and-fast-storage/.

8 F. Rosciano, P. P. Pescarmona, K. Houthoofd, A. Persoons, P. Bottke and M. Wilkening, *Phys. Chem. Chem. Phys.*, 2013, **15**, 6107–6112.

9 M. Park, X. Zhang, M. Chung, G. B. Less and A. M. Sastry, *J. Power Sources*, 2010, **195**, 7904–7929.

10 A. N. Lab, *Materials and energy flows in the materials production, assembly and end-of-life stages of the automotive lithium ion battery life cycle*, 2010.

11 A. N. Lab, *Modeling the Performance and Cost of Lithium-Ion Batteries for Electric-Drive Vehicles*, 2011.

12 P. Arora and Z. Zhang, *Chem. Rev.*, 2004, **104**, 4419–4462, DOI: 10.1021/cr020738u.

13 D. Ruzmetov, V. P. Oleshko, P. M. Haney, H. J. Lezec, K. Karki, K. H. Baloch, A. K. Agrawal, A. V. Davydov, S. Krylyuk, Y. Liu, J. Y. Huang, M. Tanase, J. Cumings and A. A. Talin, *Nano Lett.*, 2012, **12**, 505–511.

14 D. Santhanagopalan, D. Qian, T. McGilvray, Z. Wang, F. Wang, F. Camino, J. Graetz, N. Dudney and Y. S. Meng, *J. Phys. Chem. Lett.*, 2014, **5**, 298–303.

15 Y. Liu, X. H. Liu, B.-M. Nguyen, J. Yoo, J. P. S. S. T. Picraux, J. Y. Huang and S. A. Dayeh, *Nano Lett.*, 2013, **13**, 4876–4883.

16 M. M. Thackery and J. B. Goodenough, *Solid state cell wherein an anode solid electrolyte and cathode each comprise a cubic-close-packed framework structure*, US Pat., 4507371, 1985.

17 F. Rosciano, P. P. Pescarmona and A. Persoons, *Ion conductor and solid state battery*, US Pat., Application 20130045426 A1, 2013.

18 F. Rosciano, P. P. Pescarmona and A. Persoons, *218th ECS Meeting*, 2010, vol. 127.

19 M. Thackeray, L. de Picciotto, A. de Kock, P. Johnson, V. Nicholas and K. Adendorff, *J. Power Sources*, 1987, **21**, 1–8.

20 J. B. Goodenough and K.-S. Park, *J. Am. Chem. Soc.*, 2013, **135**, 1167–1176.

21 M. Thackeray, P. Johnson, L. A. de Picciotto, P. Bruce and J. Goodenough, *Mater. Res. Bull.*, 1984, **19**, 174–187.

22 R. Gummow, A. Kock and M. Thackery, *Solid State Ionics*, 1994, **69**, 59–67.

23 T. Aaltonen, V. Miikkulainen, K. B. Gandrud, A. Pettersen, O. Nilsen and H. Fjellvg, *220th ECS Meeting*, 2011.

24 K. M. Colbow, J. R. Dahn and R. R. Haering, *J. Power Sources*, 1989, **26**, 397–402.

25 M. J. Mees, G. Pourtois, F. Rosciano, B. Put, P. M. Vereecken and A. Stesmans, *Phys. Chem. Chem. Phys.*, 2013, **16**, 5399–5406.

26 H. Kawai, M. Tabuchi, M. Nagata, H. Tukamoto and A. R. West, *J. Mater. Chem.*, 1998, **8**, 1273–1280.

27 H. Lutz, W. Schmidt and H. Haeuseler, *J. Phys. Chem. Solids*, 1981, **42**, 287–289.

28 R. Kanno and Y. T. O. Yamamoto, *Mater. Res. Bull.*, 1981, **16**, 999–1005, DOI: 10.1016/0025-5408(81)90142-2.

29 S. Giangrandi, T. Sajavaara, B. Brijs, K. Arstila, A. Vantomme and W. Vandervorst, *Nucl. Instrum. Methods Phys. Res., Sect. B*, 2008, **266**, 5144–5150.

30 J. Shou-Yong, L. Li-Bin, H. Ning-Kang, Z. Jin and L. Yong, *Phys. Chem. Chem. Phys.*, 2000, **19**, 225–227.

31 M. Lejus and R. Collongues, *C.R. Chim.*, 1962, 2005–2007.

32 L. Vegards, *Z. Phys.*, 1921, **5**, 17–26.

33 F. Ayguavivesa, B. Agius, B. Ea-Kim and I. Vickridge, *J. Mater. Res.*, 2001, **16**, 3005–3008.

34 S. Berg and I. Katardjiev, *J. Vac. Sci. Technol., A*, 1999, **17**, 1916–1925.

35 S. Jakschik, U. Schroeder, T. Hecht, M. Gutsche, H. Seid and J. W. Bartha, *Thin Solid Films*, 2003, **425**, 216–220.

36 A. Rahman and M. S. Raven, *Thin Solid Films*, 1980, **71**, 7–13, DOI: 10.1016/0040-6090(80)90177-7.

37 M. Voigt and M. Sokolowski, *Mater. Sci. Eng., B*, 2004, **109**, 99–103.

38 M. Bortz, R. French, D. Jones, R. Kasowski and F. Ohuchi, *Phys. Scr.*, 1990, **41**, 537–541.

39 M. Ihara, Y. Arimoto, M. Jifuku, T. Kimura, S. Kodama, H. Yamawaki and T. Yamaoka, *J. Electrochem. Soc.*, 1982, **129**, 2569–2573, DOI: 10.1149/1.2123611.

40 H. Honbo and H. Momose, *J. Electroanal. Chem.*, 2010, **638**, 269–274.

41 R. Wibowo, S. E. Jones and R. G. Compton, *J. Phys. Chem. B*, 2009, **113**, 12293–12298.

42 R. Huggins, *Ionics*, 2002, **8**, 300–313.

43 S. C. Jung and Y. Han, *J. Phys. Chem. Lett.*, 2013, **4**, 2681–2685.

44 G. Song, X. Li, Y. Wang, Z. Peng, Y. Yu and P. Li, *Mater. Charact.*, 2010, **61**, 371–375.

45 J. Macdonald, LEVM Manual, 2015 http://jrossmacdonald.com/jrm/wp-content/uploads/LEVMMANUAL.pdf.

46 A. J. Bard and L. R. Faulkner, *Electrochemical Methods Fundamentals and Applications*, John Wiley and Sons, 2001.

47 A. C. Kozen, C.-F. Lin, A. J. Pearse, M. A. Schroeder, X. Han, L. Hu, S.-B. Lee, G. W. Rubloff and M. Noked, *ACS Nano*, 2015, **9**, 5884–5892.

48 Y. S. Jung, A. S. Cavanagh, L. A. Riley, S.-H. Kang, A. C. Dillon, M. D. Groner, S. M. George and S.-H. Lee, *Adv. Mater.*, 2010, **22**, 2172–2176.

49 X. Xiao, P. Lu and D. Ahn, *Adv. Mater.*, 2011, **23**, 3911–3915.

50 M. E. Orazem, I. Frateur, B. Tribollet, V. Vivier, S. Marcelin, N. Pebere, A. L. Bunge, E. A. White, D. P. Riemer and M. Musiani, *J. Electrochem. Soc.*, 2013, **160**, C215–C225, DOI: 10.1149/2.033306jes.